p53 drives a transcriptional program that elicits a non-cell-autonomous response and alters cell state in vivo

Sydney M. Moyer[a,b], Amanda R. Wasylishen[b], Yuan Qi[c], Natalie Fowlkes[d], Xiaoping Su[c], and Guillermina Lozano[a,b,1]

[a]Genetics and Epigenetics Program, The University of Texas MD Anderson Cancer Center UTHealth Graduate School of Biomedical Sciences, Houston, TX 77030; [b]Department of Genetics, The University of Texas MD Anderson Cancer Center, Houston, TX 77030; [c]Department of Bioinformatics and Computational Biology, The University of Texas MD Anderson Cancer Center, Houston, TX 77030; and [d]Department of Veterinary Medicine and Surgery, The University of Texas MD Anderson Cancer Center, Houston, TX 77030

Contributed by Guillermina Lozano, August 4, 2020 (sent for review May 1, 2020; reviewed by Christine M. Eischen and James J. Manfredi)

Cell stress and DNA damage activate the tumor suppressor p53, triggering transcriptional activation of a myriad of target genes. The molecular, morphological, and physiological consequences of this activation remain poorly understood in vivo. We activated a p53 transcriptional program in mice by deletion of *Mdm2*, a gene that encodes the major p53 inhibitor. By overlaying tissue-specific RNA-sequencing data from pancreas, small intestine, ovary, kidney, and heart with existing p53 chromatin immunoprecipitation (ChIP) sequencing, we identified a large repertoire of tissue-specific p53 genes and a common p53 transcriptional signature of seven genes, which included *Mdm2* but not *p21*. Global p53 activation caused a metaplastic phenotype in the pancreas that was missing in mice with acinar-specific p53 activation, suggesting non-cell-autonomous effects. The p53 cellular response at single-cell resolution in the intestine altered transcriptional cell state, leading to a proximal enterocyte population enriched for genes within oxidative phosphorylation pathways. In addition, a population of active CD8+ T cells was recruited. Combined, this study provides a comprehensive profile of the p53 transcriptional response in vivo, revealing both tissue-specific transcriptomes and a unique signature, which were integrated to induce both cell-autonomous and non-cell-autonomous responses and transcriptional plasticity.

p53 | transcriptome | signature | single-cell sequencing | Mdm2

The *p53* tumor suppressor encodes a transcription factor responsible for coordinating a stress response in cells. It acts primarily through activation of downstream target genes by binding to a specific DNA sequence (1, 2). Initiation of p53 transcriptional activity is mediated by cell stress such as DNA damage, hypoxia, and oncogenic signaling (3). p53 activates genes to facilitate distinct cellular outcomes, including but not limited to up-regulation of cell cycle arrest pathways (via target genes *Cdkn1a*, *Ccng1*), senescence (*Cdkn1a*), apoptosis (*Bbc3*, *Pmaip1*), or alternations to cell metabolism (*Tigar*) (3, 4). Moreover, the importance of this transcription factor is highlighted by the fact that wild-type p53 function is lost and/or severely dampened in most, if not all, human cancers (5, 6).

Activation of p53 target genes, out of hundreds suspected to be regulated by p53, is thought to be largely tissue, damage, and time specific (7). For example, expression of the p53 target gene *Lif* (leukemia inhibitory factor) is required in the uterus of female mice for proper embryo implantation (8). Decreased *Lif* levels in $p53^{-/-}$ mice lead to fewer and smaller litters. Additionally, a mouse model with slightly elevated p53 levels shows that animals are severely radiosensitive and succumb to a sublethal dose of ionizing radiation in ∼20 d (9). Lethality is caused by bone marrow failure and can be completely reversed by genetic loss of the p53 apoptotic target *Puma* (*Bbc3*). Conversely, loss of the cell cycle arrest and senescent p53 target gene *p21* (*Cdkn1a*) was unable to prolong the life of these mice. These studies implicate the importance of specific p53 target genes and pathways in individual tissue types; however, much is still to be learned about the p53 transcriptome as many phenotypes are observed in mouse models with elevated p53 (i.e., decreased organ weight and infertility) that still have not been fully explained (10, 11).

To identify the direct transcriptional targets of p53, multiple groups have conducted ChIP (chromatin immunoprecipitation)-sequencing studies in cell lines with exogenous p53 pathway activation. For example, Kenzelmann Broz et al. (12) identified gene promoters bound by p53 in mouse embryo fibroblasts (MEFs) treated with the DNA-damaging agent doxorubicin. Li et al. (13) identified the p53 transcriptional program in mouse embryonic stem cells treated with the DNA-damaging agent adriamycin and observed that binding of p53 to DNA correlated with gene activation. These invaluable studies were performed in in vitro systems and lack the cellular complexity of tissues and the physiology of an organism.

To gain a better understanding of how p53 functions in a tissue-specific manner, we used a genetically engineered mouse model of p53 activation, mediated by conditional deletion of *Mdm2* (14). Mdm2 is an E3 ligase and the essential negative regulator of p53, which either binds the transactivational domain

Significance

Although p53 is highly studied, the molecular and physiological consequences of the p53 transcriptional response are poorly understood. Through RNA sequencing of multiple mouse tissues upon genetic activation of p53, we identified hundreds of tissue-specific p53 target genes and a set of genes that is commonly expressed and can serve as a signature for p53 pathway activation. In the pancreas, we observed a non-cell-autonomous response while the small intestine displayed altered transcriptional cell states. Our study begins to uncover the commonalities and differences engrained in the tissue-specific and cell-specific p53 transcriptomes. Gaining a better understanding of the wild-type p53 transcriptome will subsequently lead to determining the elusive combination of genes responsible for the tumor-suppressive function of p53.

Author contributions: S.M.M., A.R.W., and G.L. designed research; S.M.M., A.R.W., Y.Q., N.F., and X.S. performed research; and S.M.M., A.R.W., and G.L. wrote the paper.

Reviewers: C.M.E., Thomas Jefferson University; and J.J.M., Icahn School of Medicine at Mount Sinai.

The authors declare no competing interest.

[1]To whom correspondence may be addressed. Email: gglozano@mdanderson.org.

This article contains supporting information online at https://www.pnas.org/lookup/suppl/doi:10.1073/pnas.2008474117/-/DCSupplemental.

First published September 8, 2020.

of p53 to inhibit its function or ubiquitinates p53 for nuclear export and/or proteasomal degradation (1, 15). Genetic loss of *Mdm2* in embryos, as well as in adult mice, up-regulates p53 and results in lethal phenotypes; however, this lethality is rescued by concomitant loss of *p53* (16–18). p53 and Mdm2 are also involved in a negative feedback loop whereby under homeostatic conditions, Mdm2 keeps p53 activity low (19). Moreover, *Mdm2* is a downstream target gene of p53, and thus, p53 transcription ultimately leads to its own degradation (20). Maintenance of this feedback loop is crucial as mice lacking the ability to up-regulate *Mdm2* through p53 are exquisitely radiosensitive (9, 21).

We profiled 13 murine tissues for p53 transcriptional activity following *Mdm2* loss and then selected 5 tissues (pancreas, heart, kidney, ovary, and intestine) that displayed a wide range of molecular and pathological responses for comprehensive analysis. We conducted RNA-sequencing analysis and a comparison with existing ChIP-sequencing data to understand the physiological response to p53 activation. We identified a unique p53 signature of seven p53 transcriptional targets that unexpectedly excludes *p21*, the quintessential p53 target used by all to assay p53 function. In addition to this small subset of overlapping genes, the overall transcriptional programs of different tissues provide insight into the downstream pathways that are induced by p53. Our data also provide evidence that the pathology observed by global activation of p53 can be non-cell-autonomous, as the metaplastic phenotype observed in the pancreas is not recapitulated with acinar-specific depletion of *Mdm2*. Finally, our studies show how p53 activation can influence and alter the transcriptional cell states present within the intestinal epithelial cells and immune compartment. Understanding the physiologically relevant pathways initiated by p53 may allow activation of tumor suppressor activity downstream of *p53* loss in tumors.

Results

p53 Transcriptional Activity after Genetic Ablation of Mdm2 In Vivo. To examine the repertoire of p53 transcriptional target genes in vivo, we used the conditional *Mdm2* allele ($Mdm2^{FM}$) and a ubiquitously expressed but tamoxifen-inducible *Cre* transgene ($CAG\text{-}CreER^{Tg}$) to generate a robust genetic model of p53 activation in C57BL/6J mice. Our experimental groups consisted of $Mdm2^{FM/-}$ $CAG\text{-}CreER^{Tg}$ (FMTg) mice, which require only a single recombination event to lose *Mdm2* in a cell, along with $Mdm2^{+/-}$ $CAG\text{-}CreER^{Tg}$ (Tg) and $Mdm2^{FM/-}$ (FM) control mice, which retain expression of *Mdm2*. In this model, three daily intraperitoneal (IP) tamoxifen injections (1.5 mg) to 2- to 4-mo-old FMTg mice induce p53-dependent morbidity on average at 4 d after the last injection (*SI Appendix*, Fig. S1) (16). Mice with concomitant loss of *p53* ($Mdm2^{FM/-}$ $p53^{-/-}$ $CAG\text{-}CreER^{Tg}$) or no transgene ($Mdm2^{FM/-}$) showed no signs of morbidity (*SI Appendix*, Fig. S1) (16). It is important to note that Tg control mice lost ~10% of their body weight after IP tamoxifen injections; thus, Cre activity alone is eliciting a biological response, highlighting the need for use of Cre-positive control mice (*SI Appendix*, Fig. S1*B*).

To study the acute p53 transcriptional program induced by *Mdm2* loss, we selected a single higher dose of tamoxifen (3 mg) and euthanized animals 24 h after IP injection (Fig. 1*A*) (22). This allowed us to capture the direct molecular changes induced by p53 activation via genetic loss of *Mdm2*. FMTg and Tg mice lost ~10% of their body weight 24 h after injection, but they were viable and displayed no other evidence of morbidity (Fig. 1*B*). Notably, Cre-negative mice (FM) displayed negligible weight loss after receiving tamoxifen (Fig. 1*B*).

We next assayed a panel of 13 tissues for p53 transcriptional activity via *p21* and *Puma* expression and recombination efficiency of the $Mdm2^{FM}$ allele (*SI Appendix*, Table S1). Recombination was determined as previously described by Zhang et al. (16). We surprisingly did not observe a significant correlation between percent recombination and transcriptional activation, suggesting that other cell- and tissue-intrinsic mechanisms regulate the p53 transcriptional program (Pearson correlation; $R^2 = 0.13$, two-tailed P value = 0.22). In addition, *p21* induction was always higher than *Puma* induction except in the brain and liver (*SI Appendix*, Table S1). Recombination and expression in tissues generally fell into four categories: high *Mdm2* recombination, high *p21* levels; high *Mdm2* recombination, low *p21* levels; low *Mdm2* recombination, high *p21* levels; and low *Mdm2* recombination, low *p21* levels. Recombination was considered high if more than 30% of the tested tissue recombined the $Mdm2^{FM}$ allele. Moreover, if the relative messenger RNA (mRNA) level of *p21* was greater than four, the tissue was considered to have high *p21* levels. Similar results were also obtained when the expression of *Puma* was used as a readout for p53 transcriptional activity (*SI Appendix*, Table S1). To profile the wide range of p53 activity, we proceeded with five tissues that fell into the four p53 activation groups: pancreas, small intestine, ovary, kidney, and heart, with two tissues (pancreas and intestine) represented in the high-recombination and high-transcriptional activation group (Fig. 1*C*).

Acute p53 Activation Results in Tissue-Specific Pathological Responses. We next conducted a more thorough molecular and histological characterization of these five tissues. The pancreas, intestine, and kidney of FMTg mice displayed significant increase of p53 protein compared with Tg tissues, which correlated well with *p21* and *Puma* mRNA increases (Fig. 1 *D*–*F*). The ovary and heart, despite recombination of *Mdm2*, showed a more modest transcriptional p53 response and lacked robust increases in p53 protein levels. Of note, Tg control mice displayed signs of p53 pathway activation, as measured by increased *p21* and *Puma* mRNA levels and p53 protein levels, compared with Cre-negative mice (*SI Appendix*, Fig. S2), suggesting that Cre activity induces a stress response. This phenomenon was most robust in the Tg pancreas.

After only 24 h, p53 activation resulted in strong morphological changes in FMTg intestine, kidney, and pancreas compared with Tg mice (Fig. 1*G*). The intestinal crypts, the invaginated region between the villi that is composed of stem cells and newly differentiated epithelial cells (23), experienced 20% crypt atrophy/dropout (Fig. 1*H*). To evaluate apoptosis of crypt epithelial cells, we assayed and quantified cleaved caspase-3 positivity and accompanying DNA damage (gamma-H2A histone variant X [γH2AX] immunohistochemistry). Throughout FMTg intestines, we could see an increased number of cells staining positive for apoptosis and DNA damage when compared with Tg intestines, likely due, in part, to increased p53 activity coupled with activation of the Cre recombinase (*SI Appendix*, Fig. S3) (24). The tubules of FMTg kidneys, structures crucial for absorption of water and electrolytes (25, 26), were dilated in response to up-regulated p53 (Fig. 1*G*). In addition, large casts of coagulated protein formed within the kidneys, and the overall number of protein casts was higher than Tg controls (Fig. 1 *G* and *I*). Structural changes to the FMTg pancreatic acinar cells were reminiscent of acinar to ductal metaplasia and had a 20% increase in area staining positively with the ductal cell marker cytokeratin 19 (CK19) (Fig. 1*J*). Additionally, FMTg pancreas displayed severe necrotizing pancreatitis with robust immune cell infiltration as evident from hematoxylin and eosin (H&E) staining (Fig. 1 *G* and *K*). Histological analysis revealed that the heart and ovary of FMTg mice did not display any noticeable morphological differences at this 24-h time point (Fig. 1*G*).

RNA Sequencing Reveals the Transcriptome Associated with Acute p53 Activation In Vivo. FMTg mice with concomitant deletion of *p53* display no signs of morbidity or gross tissue pathologies after IP tamoxifen, demonstrating that the phenotypes in FMTg mice are p53-dependent (16). Since p53 functions as a transcription factor, we employed RNA sequencing to elucidate the tissue-specific

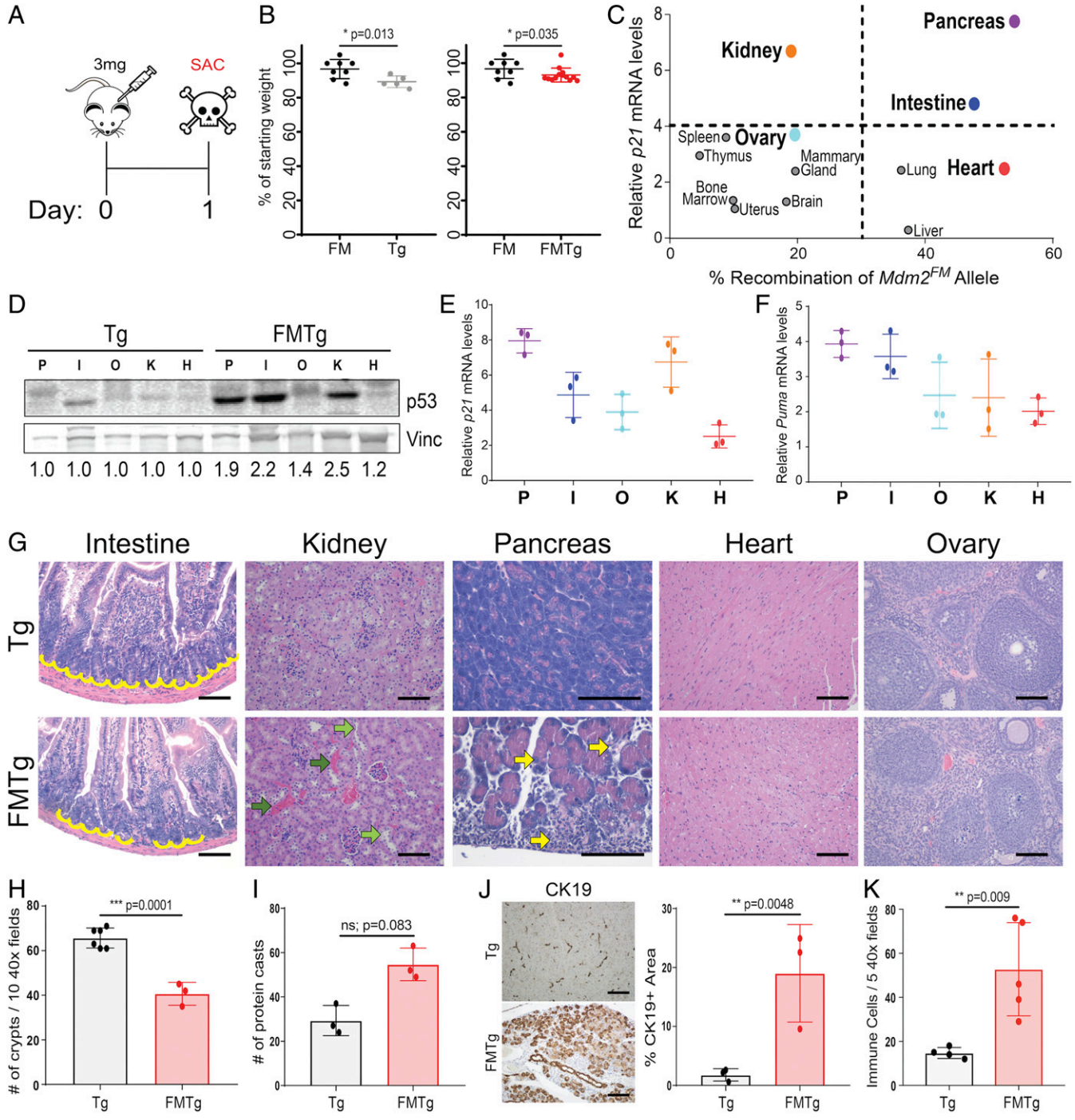

Fig. 1. Acute p53 activation in $Mdm2^{FM/-}$ $CAG\text{-}CreER^{Tg}$ mice. (*A*) Treatment regimen and time point of euthanasia (SAC). (*B*) Weight loss at euthanasia as a percent of weight on injection day in FM ($Mdm2^{FM/-}$), Tg ($Mdm2^{+/-}$ $CAG\text{-}CreER^{Tg}$), and FMTg ($Mdm2^{FM/-}$ $CAG\text{-}CreER^{Tg}$) mice with Student's *t* test for statistical analysis. (*C*) Correlation between percent recombination of the $Mdm2^{FM}$ allele and relative *p21* mRNA levels in FMTg mice normalized to Tg mice. Graph is divided into arbitrary quadrants. (*D*) Western blot for p53 protein expression compared with vinculin (Vinc). Quantification of p53/Vinc signal, relative to Tg sample within a given tissue type, is indicated below the bands. H, heart; I, intestine; K, kidney; O, ovary; P, pancreas. (*E* and *F*) qRT-PCR of tissues from FMTg mice normalized to Tg mice. Expression normalized to *Rplp0*. (*G*) H&E staining. Yellow lines, crypts; light green arrows, dilated tubules; dark green arrows, protein cast; yellow arrows, infiltrating immune cells. (Scale bars, 100 μm.) (*H*) Quantification of crypt loss in intestines of mice 24 h after tamoxifen. Numbers are total crypts counted within ten 40× fields, and dots indicate biological replicates with Student's *t* test for statistical analysis. (*I*) Number of protein casts per kidney; dots indicate biological replicates with Student's *t* test for statistical analysis. (*J*) Representative images of CK19 immunohistochemistry and quantification; dots indicate biological replicates with Student's *t* test for statistical analysis. (Scale bars, 100 μm.) (*K*) Quantification of immune cells. Number of immune cells within five 40× fields; dots indicate biological replicates. All data are presented as mean ± SD from individual mice.

transcriptional program activated by p53 in FMTg pancreas, heart, kidney, ovary, and intestine. DESeq2 analysis of five FMTg compared with three Tg tissues revealed hundreds of genes with an adjusted P value < 0.05 and thus, differentially expressed (Fig. 2*A* and Dataset S1) (27). On average, 85% of all differentially expressed genes (DEGs) were up-regulated in a given tissue, consistent with p53's primary function as a positive regulator of transcription (Fig. 2*A*) (28).

To distinguish between direct and indirect transcriptional changes, we employed previously published ChIP-sequencing data (Dataset S1) (12). These data were generated by Kenzelmann Broz et al. (12) from wild-type MEFs that were treated with the DNA-damaging agent doxorubicin to activate p53 exogenously. Overlaying our tissue-specific RNA-sequencing data with this bulk ChIP-sequencing dataset revealed the percentage of DEGs identified above that had a p53 binding site anywhere within their promoter region (differentially expressed p53 target genes) (Fig. 2*B*). The kidney and intestine have the purest p53-dependent transcriptional changes as the majority of their DEGs were direct p53 targets (kidney: 59% [77/130]; intestine: 69% [42/61]) (Fig. 2*B*). In addition, these tissues have no down-regulated DEGs overlapping with the ChIP-sequencing data, suggesting that p53 works exclusively as a transcriptional activator in these tissues at this time point (Fig. 2*C*). Only 28% (206/747) of the DEGs in FMTg pancreas were p53 target genes, and nearly 10% of those targets are down-regulated (20/206), suggesting that many of these changes may be indirect (Fig. 2*C*). The heart and ovary, tissues with no robust morphological phenotype, had the lowest portion of direct p53 target genes differentially expressed after *Mdm2* loss (heart: 16% [95/604]; ovary: 24% [21/88]) (Fig. 2*B*).

To understand what particular pathways these tissue-specific p53 target genes were involved in, we employed Gene Set Enrichment Analysis (GSEA) on Hallmark and Gene Ontology (GO) pathways (29, 30). Despite presenting different sensitivities to p53 pathway activation at the morphological level, all five of the tested FMTg tissues significantly enriched the Hallmark p53 pathway (Fig. 2*D*). Moreover, all five tissues enriched pathways that share a significant overlap with the Hallmark p53 pathway, such as response to DNA damage, response to ultraviolet radiation, and the GO cell cycle process pathway. GSEA validated that we successfully captured a p53 response in the murine pancreas, heart, kidney, ovary, and intestine and surprisingly, that the resulting DEG lists, albeit associated with vastly different tissue-specific morphological outcomes, activate similar p53-associated pathways.

A remarkable tissue specificity was also apparent. The pancreas, for example, showed that 66% of the DEGs were specific to the pancreas and not differentially expressed in other tissues (Fig. 3*A*). This is likely due to the non-cell-autonomous nature of the response in the pancreas (see below). The heart also showed that 52% of DEGs were unique and expressed only in the heart. The heart is also the only tissue to display multiple significant GSEA extracellular matrix pathways (Fig. 2*D*). The intestine showed the lowest number of unique DEGs (10%) (Fig. 3*A*).

A Common p53 Signature That Includes Mdm2 but Not p21. Only seven DEGs were commonly expressed across all tissue types: *Ccng1*, *Eda2r*, *Gtse1*, *Mdm2*, *Polk*, *Psrc1*, and *Zfp365* (Fig. 3 *A* and *B*) (*SI Appendix*, Table S2). Surprisingly, this list does not include *p21*, the gene historically used as the gold standard readout for p53 transcriptional activation. However, *p21* was significantly differentially expressed in FMTg pancreas, intestine, and kidney (the tissues with the most robust histological changes). Importantly, *Mdm2* was identified as one of the common differentially expressed target genes since deletion of *Mdm2* occurs in exons 5 and 6, leaving an intact p53 binding sequence in the promoter (14). The other common DEGs have also been previously linked to p53 activity. *Eda2r* was previously reported to be an anoikis target for p53 (32). *Gtse1* and *Psrc1* are paralogs involved in p53 cell cycle regulation along with Cyclin G1 (*Ccng1*) (33–36). *Polk* is the gene that encodes DNA Polymerase Kappa, which allows for DNA replication in the presence of DNA lesions; DNA double-strand breaks were observed in all tissues and quantified by γH2AX staining as indicated above (*SI Appendix*, Fig. S3) (37, 38). Finally, *Zfp365* is a zinc-finger protein required for proper resolution of DNA double-strand breaks (39).

Furthermore, ChIP-qPCR experiments of FMTg pancreas validated binding of p53 at the promoters of all seven genes in p53 antibody ChIPs compared with Immunoglobulin G (IgG) antibody ChIPs (Fig. 3*C*). Additionally, the binding to these seven genes was enriched over p53 binding at the *Chrm5* promoter; *Chrm5* encodes acetylcholine receptor and is not bound by p53, and thus, it serves as a negative control for this assay (40). Thus, the functions of these seven genes embody the pathways found via GSEA and have been experimentally validated as p53 target genes through ChIP-qPCR.

To determine if these seven genes could serve as a signature for wild-type p53 transcriptional activation in other settings, we exogenously activated p53 by utilizing ionizing radiation (IR) to induce DNA damage (41). A sublethal dose (6 gray) of IR was administered to both wild-type ($n = 3$) and $p53^{-/-}$ ($n = 5$) BALB/c mice, while unirradiated wild-type BALB/c mice ($n = 2$) served as controls. All mice were euthanized 4 h after IR exposure when p53 protein is highest (9). The seven genes showed robust transcriptional activation after IR, in a p53-dependent manner, with the kidney showing, consistently, the highest activation of all seven genes after IR (Fig. 4*A*). Additionally, the use of *p53*-null mice allowed us to determine if other transcription factors can activate expression of these genes post-IR. In fact, there was up-regulation of *Gtse1* in three of five irradiated *p53*-null pancreas samples. However, this phenomenon did not occur in other tissues (*SI Appendix*, Fig. S4).

Following IR, all five tissues tested showed moderate increases in p53 protein levels, with the intestine and ovary having the highest levels and heart having the lowest (Fig. 4*B*). To directly compare p53 protein levels elevated in response to *Mdm2* loss or IR, we performed a western blot for total p53 protein in the kidneys (Fig. 4*C*). The kidneys are of particular interest since they had the highest induction of our gene signature in a p53-dependent manner. Furthermore, in our FMTg model, the kidney displayed robust tubule dilation and protein cast formation despite having "low" recombination of *Mdm2*. Loss of *Mdm2* increased p53 protein to considerably higher levels (average four times) than that of IR (average two times) (Fig. 4*C*). Since p53 is highly posttranslationally modified following cell stress such as the DNA damage induced by IR (42, 43), we speculated that phosphorylation of p53 may differ in the kidney after *Mdm2* loss compared with IR. We observed significant phosphorylation of p53 at serine-15 only in irradiated kidney samples (average four times) (Fig. 4*C*). Further studies are needed in other tissues to understand the intricacies of p53 posttranslational modifications and how this affects p53 transcriptional activity. In summary, the fact that seven genes (*Ccng1*, *Eda2r*, *Gtse1*, *Mdm2*, *Polk*, *Psrc1*, and *Zfp365*) are transcriptionally up-regulated in multiple tissues, within two different mouse strains, in response to p53 activation genetically (*Mdm2* loss) and exogenously (IR), indicate that they can serve as a universal signature for transcriptional activation by wild-type p53.

The Pancreatic Response to p53 Activation in FMTg Mice Is Non-Cell-Autonomous. The FMTg pancreas showed a large infiltration of immune cells (Fig. 1*G*) and a metaplastic phenotype that is caused by inflammation (44). This, in combination with the small number of direct p53 targets in our RNA-sequencing data, led us to hypothesize that the pancreas was responding to ubiquitous

A

Tissue	Total # DEGs	Upregulated (%)	Downregulated (%)
Pancreas	747	580 (77.6)	167 (22.4)
Heart	604	531 (87.9)	73 (12.1)
Kidney	130	117 (90.0)	13 (10.0)
Ovary	88	74 (84.1)	14 (15.9)
Intestine	61	57 (93.4)	4 (6.6)

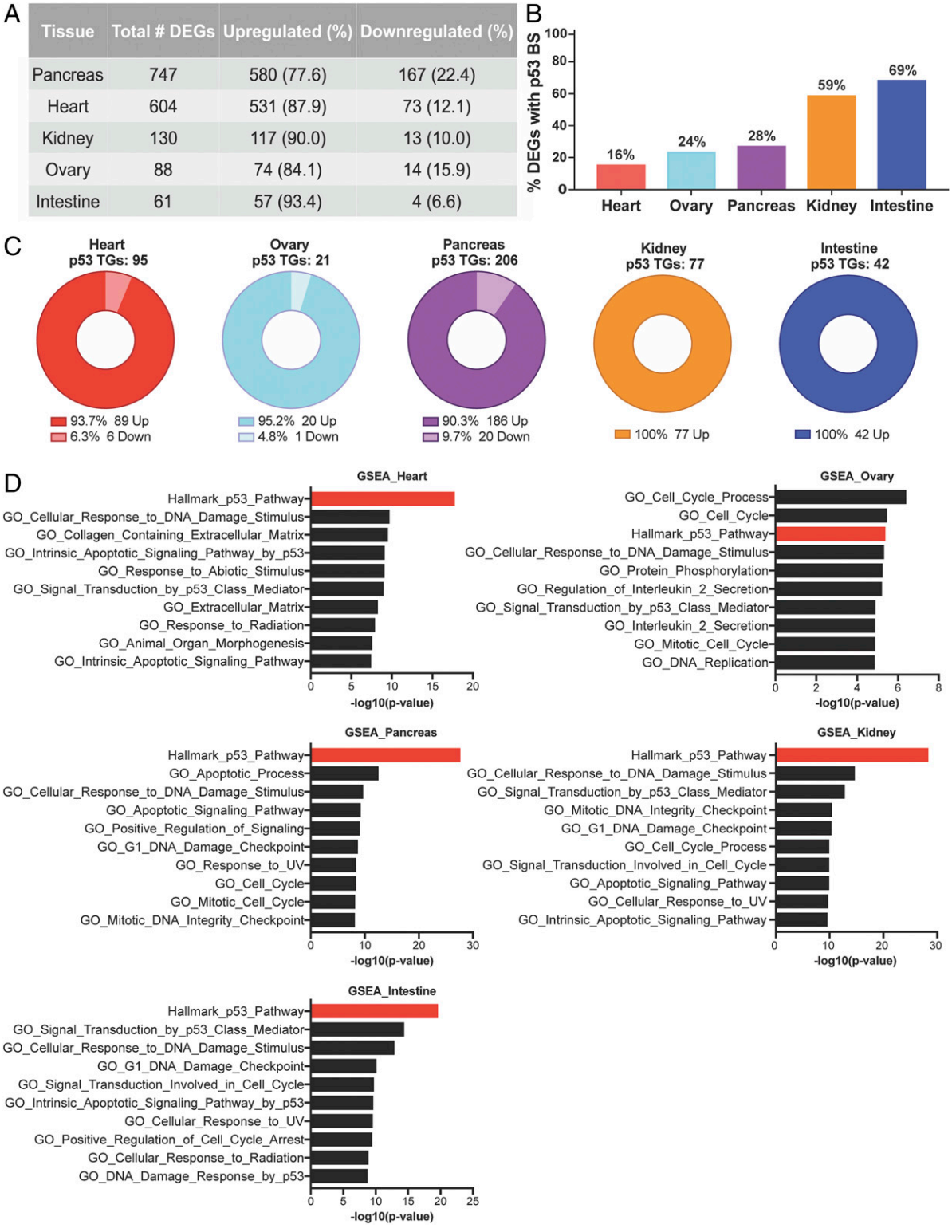

Fig. 2. RNA and ChIP-sequencing data reveal acute p53 transcriptional response. (*A*) Table depicting the total number of DEGs that resulted from DESeq2 analysis of bulk RNA-sequencing data of five tissues after p53 activation. DEGs have a *P* value of <0.05. (*B*) Bar graph depicting the percentage of total DEGs per tissue that have a p53 binding site (BS) anywhere within their promoter as per Kenzelmann Broz et al. (12) ChIP-sequencing data. These genes are henceforth referred to as differentially expressed p53 target genes. (*C*) Pie graphs depicting the percentage of up-regulated and down-regulated differentially expressed p53 target genes (TGs) for each tissue. (*D*) Top 10 enriched pathways from GSEA analysis of Hallmark and GO pathways for differentially expressed p53 target genes in FMTg. Red bars highlight the Hallmark p53 pathway in each dataset.

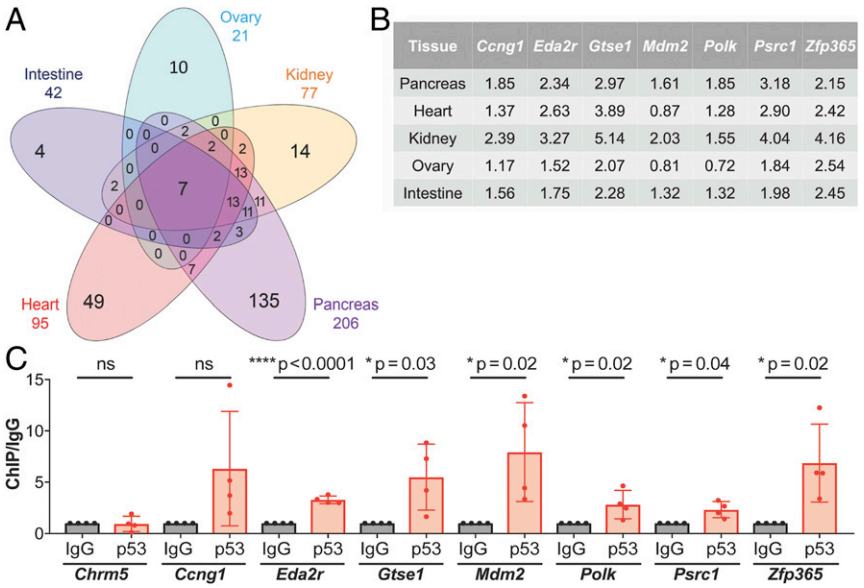

Tissue	*Ccng1*	*Eda2r*	*Gtse1*	*Mdm2*	*Polk*	*Psrc1*	*Zfp365*
Pancreas	1.85	2.34	2.97	1.61	1.85	3.18	2.15
Heart	1.37	2.63	3.89	0.87	1.28	2.90	2.42
Kidney	2.39	3.27	5.14	2.03	1.55	4.04	4.16
Ovary	1.17	1.52	2.07	0.81	0.72	1.84	2.54
Intestine	1.56	1.75	2.28	1.32	1.32	1.98	2.45

Fig. 3. Activation of p53 up-regulates a p53 signature. (*A*) Venn diagram, generated using InteractiVenn, overlaying the differentially expressed p53 target genes for each tissue (31). (*B*) Log_2 fold change values for the seven overlapping p53 target genes in *A*. (*C*) ChIP-qPCR for FMTg ($Mdm2^{FM/-}$ $CAG\text{-}CreER^{Tg}$) pancreas ($n = 4$) of seven overlapping p53 target genes presented as p53 ChIP/IgG ChIP. *Chrm5* encodes an acetylcholine receptor that serves as a negative control for p53 binding. ns, not significant. Student's *t* test was used for statistical analysis.

organismal stress from p53 activation and that these morphologic changes were not due to p53 activation in the pancreas specifically. To address this in a cell-specific manner, we crossed $Mdm2^{FM/-}$ mice to the tamoxifen-inducible and acinar cell-specific $Mist1^{CreERT2}$ to generate a small cohort of FMMist mice ($Mdm2^{FM/-}$ $Mist1^{CreERT2}$) and Mist controls ($Mdm2^{+/-}$ $Mist1^{CreERT2}$) that retained *Mdm2* expression after IP tamoxifen injections (45). An acinar-specific Cre was used because acinar cells transdifferentiate into CK19+ ductal cells upon stress, resulting in a metaplastic phenotype (44).

A small time course study was conducted to determine the tamoxifen dosing regimen necessary to achieve *Mdm2* recombination with the $Mist1^{CreERT2}$ allele that was comparable with that obtained with the $CAG\text{-}CreER^{Tg}$ allele. One week after four daily 1.5-mg IP tamoxifen injections, analysis of the FMMist pancreas showed recombination of the $Mdm2^{FM}$ allele in ∼55% of cells, similar to that achieved in the FMTg pancreas 24 h after a 3-mg tamoxifen injection (Fig. 5 *A* and *B*). To check for p53 transcriptional activity, we evaluated two genes that were among the highest significantly DEGs in FMTg pancreas RNA-sequencing data, *Eda2r* and *Gtse1* (Fig. 3*B*). In fact, qRT-PCR experiments showed that induction of *Eda2r* and *Gtse1* mRNA levels was similar in FMMist and FMTg pancreas samples (Fig. 5*C*). Moreover, similar induction of all seven genes in our proposed signature was observed in FMMist compared with Mist pancreases (*SI Appendix*, Fig. S5). Despite comparable recombination and significant p53 transcriptional activation, FMMist pancreas looked morphologically normal and displayed no signs of immune cell infiltration or metaplasia compared with Mist controls (Fig. 5 *D* and *E*). The use of this acinar cell-specific Cre indicated that the robust morphological alterations seen in FMTg pancreas were influenced by the global activation of p53 throughout the tissue and/or entire organism.

The p53 Pathway Alters Transcriptional Cell State in the Intestine. To determine how p53 activation can affect individual cell populations, we employed single-cell RNA sequencing (scRNA-seq) to evaluate the p53 transcriptome at the cellular resolution. The intestine of FMTg mice displayed the purest p53 transcriptional program. The intestine is a highly proliferative tissue that recombined the $Mdm2^{FM}$ allele in ∼50% of cells, which resulted in significant crypt dropout, induced cell death, increased DNA damage, and increased p53 protein levels and transcriptional activity. Additionally, ∼70% of DEGs in the intestine have p53 binding sites anywhere within their promoter region, and thus, the intestine was the best tissue in our model to use for scRNA-seq analysis to determine how different cell types and cell states were affected by acute p53 activation.

scRNA-seq on one male FMTg and one male Tg intestine samples resulted in ∼3,000 cells for each group that passed quality control (Fig. 6 *A*, *i*). Using the R-package Seurat, cells were clustered into 13 transcriptionally distinct cell populations capturing both immune and intestinal cell types based on previously published cell type-specific gene markers (Fig. 6 *A*, *ii* and *iii*) (*SI Appendix*, Fig. S6) (46–50). The portion of goblet, paneth, tuft, and distal enterocytes was markedly decreased after p53 activation, consistent with the high amount of quantifiable cell death in this tissue (Fig. 6*B*) (*SI Appendix*, Fig. S3). Additionally, the memory CD4+ T cell population was decreased in FMTg mice. The total numbers of enterocytes and T cells were similar in both intestinal samples, but interestingly, there was a proximal enterocyte cell population (proximal enterocytes 2) and a CD8+ T cell population (CD8+ T cells 2) that were enriched in FMTg intestines (Fig. 6 *C* and *D*). By extracting the top 100 genes that distinguish these clusters from neighboring clusters, we were able to run GSEA to see what Hallmark and/or GO pathways were subsequently enriched due to p53 activation (Dataset S1). The top 10 pathways from this analysis showed that this population of proximal enterocytes in FMTg intestines is transcribing genes associated with oxidative phosphorylation (Fig. 6*E*). In fact, GSEA shows several pathways in this enterocyte population that are associated with mitochondria and metabolism, suggesting that this population of proximal enterocytes may be more metabolically active. Additionally, the CD8+ T cell population that was prominently displayed in the FMTg intestine had only 56 significant genes that distinguished it from other T cell populations. GSEA on these 56 genes identified multiple pathways

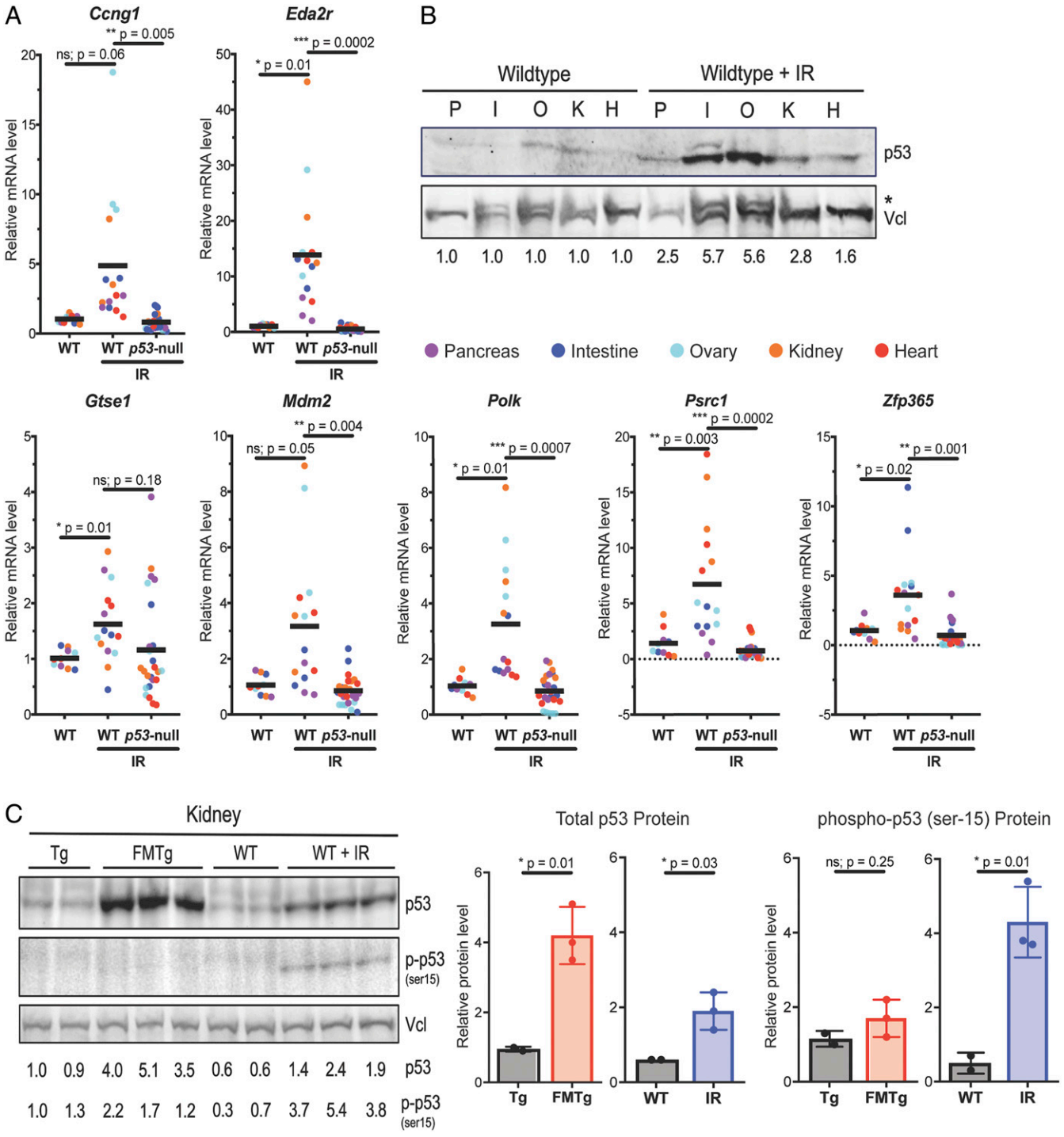

Fig. 4. Exogenous activation of p53 through IR. (*A*) qRT-PCR of irradiated (IR) wild-type (WT; $n = 3$) and *p53*-null ($n = 5$) pancreas, heart, kidney, ovary, and intestine compared with unirradiated WT ($n = 2$) for seven overlapping p53 target genes. Expression normalized to *Rplp0*. Statistical analysis was conducted with ANOVA utilizing Dunnett's test for multiple comparisons against irradiated WT mice. All data are presented as mean from individual mice. (*B*) Western blot for p53 protein expression compared with vinculin (Vcl). Quantification of p53/Vcl signal, relative to WT sample within a given tissue type, is indicated below the bands. H, heart; I, intestine; K, kidney; O, ovary; P, pancreas. *Nonspecific band. (*C*) Western blot for p53 and phosphorylated p53 at serine 15 (p-p53 ser15) and Vcl. Quantification of p53 or p-p53/Vcl signal, relative to first Tg sample, is indicated below the bands and graphed to the right with Student's *t* test for statistical analysis. ns, not significant. Data are presented as mean ± SD from individual mice.

enriched that signified that this population of T cells was "active" compared with the other T cell clusters (Fig. 6*F*). The active CD8+ T cell population was likely recruited to the intestine due to the high p53-induced cell death in this organ. These cell-state changes were dependent on p53 pathway activation as the Tg intestine sample had significantly fewer cells contributing to these populations and all other cell populations were similar between FMTg and Tg intestine (Fig. 6 *A*, *iii*).

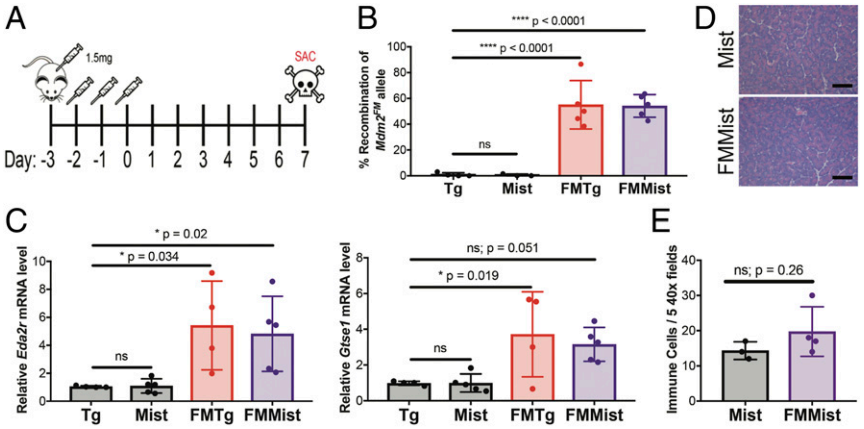

Fig. 5. The pancreatic response to p53 activation in FMTg mice is non-cell-autonomous. (*A*) Treatment regimen and time point of euthanasia (SAC) for FMMist (*Mdm2*$^{FMI-}$ *Mist1*^{CreERT2}) and Mist (*Mdm2*$^{+/-}$ *Mist1*^{CreERT2}) mice. (*B*) Percent recombination of the conditional *Mdm2*^{FM} allele as determined via qPCR assay in Mist, Tg (*Mdm2*$^{+/-}$ *CAG-CreER*^{Tg}), FMMist, and FMTg (*Mdm2*$^{FM/-}$ *CAG-CreER*^{Tg}) mice. Statistical analysis was conducted with ANOVA utilizing Dunnett's test for multiple comparisons against Tg mice. (*C*) qRT-PCR for relative *Eda2r* and *Gtse1* mRNA levels within the pancreas of Mist, Tg, FMMist, and FMTg mice. Expression normalized to *Rplp0*. Statistical analysis was conducted with ANOVA utilizing Dunnett's test for multiple comparisons against Tg mice. ns, not significant. (*D*) H&E staining on pancreas samples. (Scale bars, 100 μm.) (*E*) Quantification of immune cells. Number of immune cells within five 40× fields; dots indicate biological replicates with a Student's *t* test for statistical analysis. ns, not significant. All data are presented as mean ± SD from individual mice.

Discussion

The p53 transcription factor is responsible for orchestrating a cellular response to all types of cell stress, and thus, it is not surprising that it has the capability of activating hundreds of genes in vivo (51). However, the physiological consequences of the p53 transcriptional program, both on a tissue-specific level and on a cell-specific level, had not been studied (7, 16). A greater understanding of wild-type p53 function is warranted as the p53 pathway is altered in most, if not all, human tumors. Understanding the genes responsible for p53 function in a given tissue may lead to activation of specific downstream pathways and tumor suppression in various cancers. Our in vivo studies employ a genetic model of p53 activation and have provided crucial insight into the physiological p53 transcriptome. While the majority of p53 target genes were up-regulated in our system, small percentages of DEGs in the heart (6.3%), ovary (4.8%), and pancreas (9.7%) were direct p53 targets and down-regulated in FMTg mice, suggesting an in vivo role for p53 repression. However, these genes were not independently validated. Utilizing this model, we were able to capture hundreds of tissue-specific and seven common p53 target genes by comparison of tissue-specific bulk RNA-sequencing data with existing ChIP-sequencing data obtained from MEFs (12).

The seven common DEGs identified—*Ccng1*, *Eda2r*, *Gtse1*, *Mdm2*, *Polk*, *Psrc1*, *Zfp365*—were validated both as p53 target genes at the ChIP-qPCR level and as readouts of p53 activity post-IR. This signature validated the importance of the p53-Mdm2 feedback loop. Within 24 h of loss of *Mdm2* from a cell, p53 initiated transcription of *Mdm2* in attempts to regain balance within the system.

Three of the seven genes identified are associated with p53 regulation of the cell cycle: *Ccng1*, *Gtse1*, and *Psrc1* (33–36). *p21*, the first identified p53 transcriptional target that encodes a cell cycle inhibitor and driver of senescence (52, 53), was differentially expressed only in FMTg pancreas, intestine, and kidney. In fact, all tissues, except the heart, had pathways directly associated with the cell cycle, suggesting that proliferative tissues may have higher expression of cell cycle genes at the 24-h time point compared with tissues with lower turnover rates such as the heart. However, the overwhelming prevalence of cell cycle genes in four of five tissues insinuates that the role of p53 in cell cycle regulation may transcend cell and tissues types. More studies are needed to understand exactly how the cell cycle is being perturbed. Additionally, it is possible that our 24-h time point may have led us to capture more p53-dependent cell cycle genes.

The juxtaposition of our ubiquitous *CAG-CreER* transgene data and acinar cell-specific *Mist1*-driven Cre exposed the non-cell-autonomous nature of the p53 response (45). The FMTg pancreas exhibited a robust metaplastic phenotype after loss of *Mdm2*, while FMMist did not. Metaplasia develops in the pancreas as a response to inflammation or outside stress (44). Thus, we hypothesize that the concurrent intestinal defects may be releasing endotoxins that cause a metaplastic pancreas (54, 55). In fact, one of the genes in our signature, *Eda2r*, is a cell surface receptor, suggesting a possible role in cell–cell communication (56). Results such as these arise from studying the animal as an entire system.

scRNA-seq data were generated to better understand the p53 pathway response at a single-cell level within a tissue. We utilized FMTg intestine for this experiment since within the 24-h time period, the intestine displayed a remarkable crypt dropout phenotype and also had the highest percentage of DEGs with p53 binding sites. Activation of p53 is correlated with loss of multiple different cell populations in the murine intestine, which links nicely with the robust cell death phenotype quantified by immunohistochemistry. p53 also altered the transcriptional state of some intestinal cell populations. Loss of *Mdm2* in FMTg mice increased a population of proximal enterocytes that are transcribing oxidative phosphorylation genes, thus potentially undergoing a metabolic shift in response to p53 activation as evident by the increased expression of genes within oxidative phosphorylation pathways compared with other enterocyte populations contained within Tg intestine. However, the total number of enterocytes between Tg and FMTg mice was the same, indicating that this FMTg-specific cluster of enterocytes is driven by p53-dependent transcriptional differences. Additionally, a larger population of active CD8+ T cells was present in FMTg intestine compared to Tg intestine. These data suggest that p53 plays a role in driving activation of intestinal T cells or that activated T cells are being recruited to the FMTg intestine because of increased p53-dependent cell death.

These studies have uncovered the physiological genes and pathways regulated by p53 in vivo. A deeper understanding of how p53 responds on a cell- and tissue-specific basis is important toward understanding its role in tumor suppression.

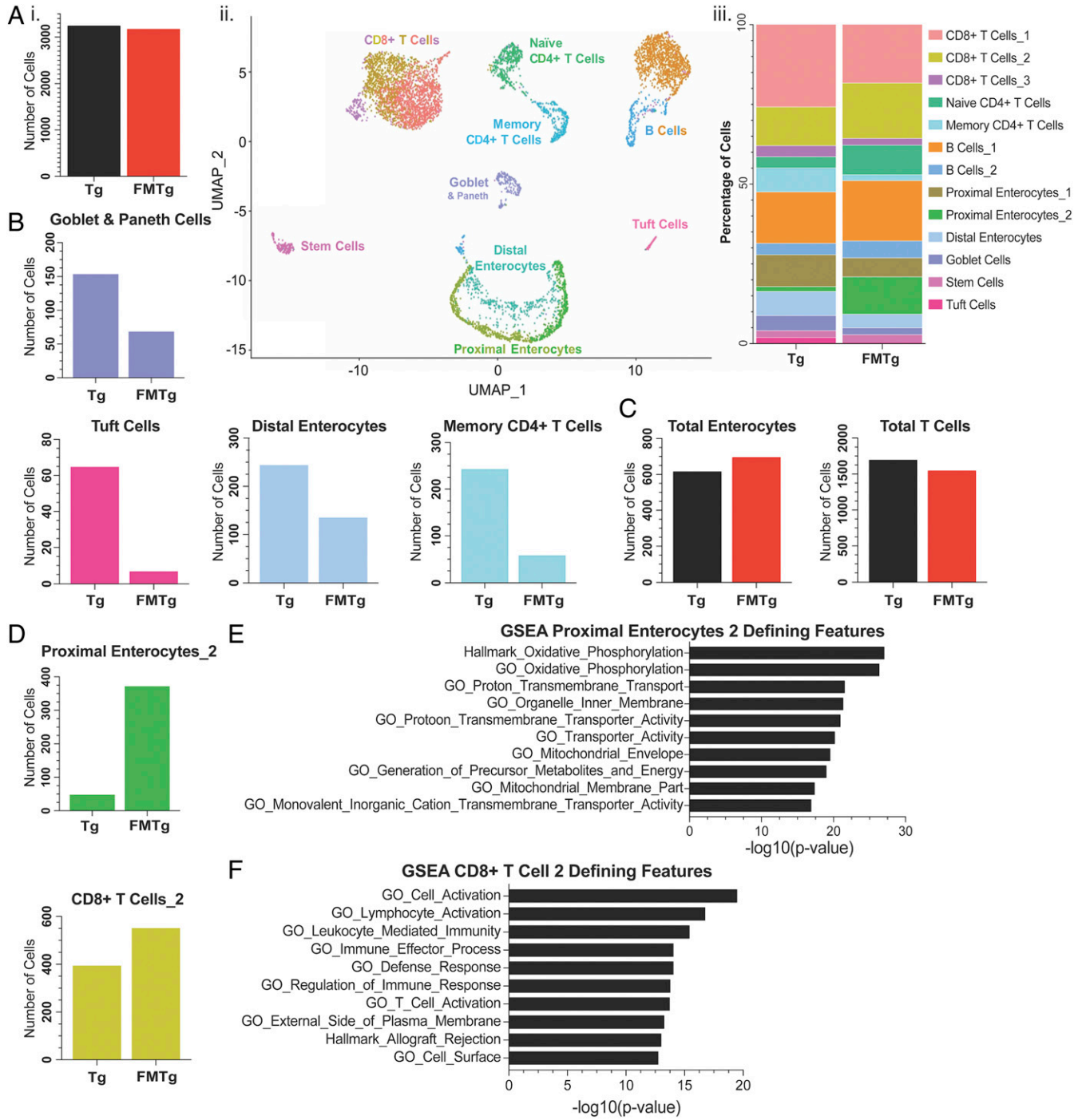

Fig. 6. scRNA-seq in FMTg intestines provides insight into cell-states driven by p53 activation. (*A*, *i*) Total number of cells analyzed after quality control metrics ran with Seurat V3 for one FMTg (*Mdm2*$^{FMI-}$ *CAG-CreER*^{Tg}) intestine sample and one Tg (*Mdm2*$^{+/-}$ *CAG-CreER*^{Tg}) intestine sample. (*A, ii*) Uniform Manifold Approximation and Projection (UMAP) of labeled cell populations. (*A, iii*) Portion of specific cell populations in FMTg and Tg samples. (*B*) Total number of goblet and paneth, tuft, distal enterocytes, and memory CD4+ T cells in FMTg and Tg intestines. (*C*) Total number of all enterocytes and T cells per group. (*D*) Number of cells that encompass proximal enterocyte population 2 and CD8+ T cell population 2 in each intestine sample. (*E*) GSEA analysis on defining features for proximal enterocyte population 2. (*F*) GSEA analysis on defining features for CD8+ T cell group 2.

Materials and Methods

Mouse Breeding, Maintenance, and Genotyping. *Mdm2*$^{FMI-}$, *Mdm2*$^{+/-}$, *Mist1*^{CreERT2}, and *CAG-CreER*^{Tg} mice have been described previously and were maintained in >90% C57BL/6J background (16, 45). *Mist1*^{CreERT2} (stock no. 029228) and *CAG-CreER*^{Tg} (stock no. 004453) mice were originally purchased from the Jackson Laboratory. Wild-type and *p53*$^{-/-}$ mice were maintained in >90% BALB/c background. All mouse studies were conducted in compliance with the National Institutes of Health guidelines for animal research and approved by the MD Anderson Cancer Center Institutional Animal Care and Use Committee. Genotyping was carried out as described earlier through PCR amplification followed by resolution on an agarose gel (57).

Protein Analysis. Protein lysates were prepared by lysing frozen pulverized tissue in 1× loading buffer. DNA was sheared using a sonicator, and samples

were boiled at 95 °C for 10 min to denature protein. Protein lysates were resolved on 10% sodium dodecyl sulfate/polyacrylamide gel electrophoresis (SDS/PAGE) gels and immunoblotted with antibodies against p53 (FL393, sc06243; Santa Cruz or CM5, P53-CM5P-L; Leica Biosystems), phosphorylated p53 at serine-15 (9284; Cell Signaling Technology), vinculin (V9131; Sigma-Aldrich), and γ-Tubulin (ab11317; Abcam). Western blots were repeated at least three times with biological replicates. Images of western blots were obtained on either the LI-COR Odyssey or Bio-Rad ChemiDoc MP imager system. Protein signal was quantified with ImageJ software (NIH). Pixel density was calculated for each band and corresponding background using the same size frame. Frame size remained the same for all bands of a given protein (row). Background signal was subtracted from protein band signal to obtain the net signal for each band. The net signal for the protein of interest was then divided by the net signal of the corresponding loading control to generate a ratio of signal strength for each sample.

Real-Time qRT-PCR. RNA was extracted from frozen, pulverized murine tissues using TRIzol reagent (Invitrogen) and then reverse transcribed using the iScript complementary DNA (cDNA) synthesis kit (Biorad). qRT-PCR was carried out as previously described using SYBR green (Bimake) on the CFX384 Touch Real-Time PCR Detection System (Biorad) (58). Expression was normalized to *Rplp0*. Primer sets are located within *SI Appendix*, Table S3.

Statistical Analysis. All data are presented as mean ± SD. All analyses were performed using GraphPad Prism V8 software. P value < 0.05 was considered significant ($^*P < 0.05$; $^{**}P < 0.01$; $^{***}P < 0.001$). Two groups were compared using a Student's t test, and multiple groups were compared using ANOVA with Dunnett's correction for multiple comparisons. Survival curve comparisons were made using a log-rank Mantel–Cox test.

Histopathology and Immunohistochemistry. Tissues harvested from mice were fixed in 10% neutral buffered formalin saline and paraffin embedded. Tissue processing, paraffin embedding, 5-μm sectioning, and H&E staining were performed by the MD Anderson Department of Veterinary Medicine and Surgery Histology Laboratory. Immunohistochemistry was performed using standard methods with citrate buffer or Tris-EDTA (ethylenediaminetetraacetic acid), pH 9.0, for 30 min of antigen retrieval. Slides were stained with antibodies against CK19 (ab133496; Abcam), cleaved caspase-3 (9664; Cell Signaling), and γH2AX (MA5-33062; ThermoFisher Scientific). Visualization was performed using ABC and DAB kits (Vector Laboratories), and hematoxylin was used as the counterstain. Slides were examined by light microscopy.

RNA Sequencing and Analysis. RNA samples were used to generate a next generation sequencing library composed of random fragments that represent the entire sample. Library preparation is automated using the Eppendorf EPMotion 5075 or the Agilent Bravo Liquid Handlers. The library is quantified by qRT-PCR, and quality control is validated using the Agilent TapeStation. The cDNA library was then ran with 10 samples per lane on the Illumina HiSeq4000 platform, generating 76-bp paired end reads. Reads were aligned to the GRCm38.p6 using STAR (version 2.6.ob) (59). Samtools (v1.8) then sorted reads and calculated mapping statistics (60). The quality of the FASTQ reads was verified using Program FastQC (0.11.5). GENCODE M19 (Ensembl 94) was employed for annotation of genes (61). DEGs were called using R (3.5.1) and Bioconductor package DESeq2 (27). DESeq2 carried out read count filtering, normalization, dispersion estimation, and identification of differential expression. DESeq2 modeled the counts using a negative binomial distribution, followed by the Wald test. The final P value was adjusted using the Benjamini and Hochberg method.

ChIP-qPCR. ChIP on FMTg pancreas samples was based on previously published protocols (40). Briefly, 200 mg of flash-frozen pancreas tissue was crushed with liquid nitrogen. Tissue was then subject to formaldehyde cross-linking for 10 min with proteinase inhibitors, and cross-linking was quenched for 5 min by the addition of glycine. Tissues were then Dounce homogenized to obtain single cells. Cells were resuspended in 750 μL of ice-cold immunoprecipitation buffer (100 mM Tris, pH 8.6, 0.3% sodium dodecyl sulfate [SDS], 1.7% Triton X-100, 5 mM ethylenediaminetetraacetic acid [EDTA]) and sonicated to an average length of 300 bp (confirmed by agarose gel electrophoresis) by pulsing 40 times for 30 s followed by 30 s of rest and 50% amplitude on a sonicator. Immunoprecipitations were performed with ~1 mg of protein and conducted in technical triplicates. Antibodies used were p53 (CM5; Leica) and Normal Rabbit IgG (2729; Cell Signaling Technology). Antibodies were incubated overnight at 4 °C. Immunoprecipitations were then incubated for 2 h with magnetic Protein G and A Dynabeads (ThermoFisher Scientific; 10001D and 10003D). ChIP washes and elusions were carried out exactly as previously described (40). qPCR was carried out as previously described using SYBR green (Bimake) on the CFX384 Touch Real-Time PCR Detection System (Biorad) (58). Primer sets are located within *SI Appendix*, Table S3.

scRNA-Seq and Analysis. Murine small intestines were isolated and rinsed with cold sterile 1× phosphate-buffered saline. Dissociation of single cells was carried out as previously described (62). Following single-cell dissociation, samples were transferred to The University of Texas MD Anderson Cancer Center Cancer Prevention and Research Institue of Texas SINGLE CORE single-cell sequencing facility, which utilizes the 10× Chromium Controller from 10× Genomics; 10,000 FMTg and 10,000 Tg small intestine cells were put through the 10× genomics pipeline. Libraries were sequenced on Illumina NovaSeq 6000 at The University of Texas MD Anderson Cancer Center Advanced Technology Genomics Core. Raw sequencing data were then returned to the SINGLE CORE for demultiplexing, alignment, and unique molecular identifier collapsing using the Cellranger tool kit from 10× Genomics. Data were then returned to our laboratory, where we used the Seurat (V3.0) R tool kit for single-cell genomics analysis to perform quality control, analysis, and evaluation of our single-cell datasets as previously described (47, 48, 50). Cells were excluded if they had fewer than 200 features or more than 30% mitochondrial gene contamination. A high level of mitochondrial gene contamination was expected in the murine intestine due to the high turnover rate of this tissue. Using the Jackstraw R package, we identified eight significant principal components, and scores from these components were used for input in downstream analyses. Visualization was performed using the UMAP function in the Seurat (V3.0) R package.

Data Availability. RNA-sequencing and scRNA-seq data were deposited in National Center for Biotechnology Information's Gene Expression Omnibus (accession nos. GSE151571 and GSE152587, respectively).

ACKNOWLEDGMENTS. We thank Aislyn Schalck and members of the laboratory of G.L. for helpful discussions. This research was supported by NIH Grant CA47296 (to G.L.), Cancer Prevention and Research Institute of Texas Integrated Single Cell Genomics Core Facility Grant RP180684, and Cancer Center Support Grant to MD Anderson Cancer Center CA16672 (it partially supports The MD Anderson Advanced Technology Genomics Core, which conducted all sequencing). S.M.M. was supported in part by the Dr. John J. Kopchick Fellowship and the American Legion Auxiliary Fellowship for Cancer Research.

1. K. H. Vousden, C. Prives, Blinded by the light: The growing complexity of p53. *Cell* **137**, 413–431 (2009).
2. S. E. Kern *et al.*, Identification of p53 as a sequence-specific DNA-binding protein. *Science* **252**, 1708–1711, 10.1126/science.2047879 (1991).
3. T. Riley, E. Sontag, P. Chen, A. Levine, Transcriptional control of human p53-regulated genes. *Nat. Rev. Mol. Cell Biol.* **9**, 402–412 (2008).
4. K. Bensaad *et al.*, TIGAR, a p53-inducible regulator of glycolysis and apoptosis. *Cell* **126**, 107–120 (2006).
5. M. Olivier *et al.*, Recent advances in p53 research: An interdisciplinary perspective. *Cancer Gene Ther.* **16**, 1–12 (2009).
6. T. Hernandez-Boussard, P. Rodriguez-Tome, R. Montesano, P. Hainaut, IARC p53 mutation database: A relational database to compile and analyze p53 mutations in human tumors and cell lines. International Agency for Research on Cancer. *Hum. Mutat.* **14**, 1–8 (1999).
7. J. G. Jackson, S. M. Post, G. Lozano, Regulation of tissue- and stimulus-specific cell fate decisions by p53 in vivo. *J. Pathol.* **223**, 127–136 (2011).
8. W. Hu, Z. Feng, A. K. Teresky, A. J. Levine, p53 regulates maternal reproduction through LIF. *Nature* **450**, 721–724 (2007).
9. V. Pant *et al.*, The p53-Mdm2 feedback loop protects against DNA damage by inhibiting p53 activity but is dispensable for p53 stability, development, and longevity. *Genes Dev.* **27**, 1857–1867 (2013).
10. V. Pant *et al.*, Distinct downstream targets manifest p53-dependent pathologies in mice. *Oncogene* **35**, 5713–5721 (2016).
11. S. M. Mendrysa *et al.*, mdm2 Is critical for inhibition of p53 during lymphopoiesis and the response to ionizing irradiation. *Mol. Cell. Biol.* **23**, 462–472 (2003).
12. D. Kenzelmann Broz *et al.*, Global genomic profiling reveals an extensive p53-regulated autophagy program contributing to key p53 responses. *Genes Dev* **27**, 1016–1031 (2013).
13. M. Li *et al.*, Distinct regulatory mechanisms and functions for p53-activated and p53-repressed DNA damage response genes in embryonic stem cells. *Mol. Cell* **46**, 30–42 (2012).

14. J. D. Grier, W. Yan, G. Lozano, Conditional allele of mdm2 which encodes a p53 inhibitor. *Genesis* **32**, 145–147 (2002).
15. S. M. Moyer, C. A. Larsson, G. Lozano, Mdm proteins: Critical regulators of embry ogenesis and homeostasis. *J. Mol. Cell Biol.* **9**, 16–25 (2017).
16. Y. Zhang *et al*., Tissue-specific and age-dependent effects of global Mdm2 loss. *J. Pathol.* **233**, 380–391 (2014).
17. R. Montes de Oca Luna, D. S. Wagner, G. Lozano, Rescue of early embryonic lethality in mdm2-deficient mice by deletion of p53. *Nature* **378**, 203–206 (1995).
18. S. N. Jones, A. E. Roe, L. A. Donehower, A. Bradley, Rescue of embryonic lethality in Mdm2-deficient mice by absence of p53. *Nature* **378**, 206–208 (1995).
19. J. C. Marine *et al*., Keeping p53 in check: Essential and synergistic functions of Mdm2 and Mdm4. *Cell Death Differ.* **13**, 927–934 (2006).
20. Y. Barak, E. Gottlieb, T. Juven-Gershon, M. Oren, Regulation of mdm2 expression by p53: Alternative promoters produce transcripts with nonidentical translation potential. *Genes Dev.* **8**, 1739–1749 (1994).
21. V. Pant, G. Lozano, Dissecting the p53-Mdm2 feedback loop in vivo: Uncoupling the role in p53 stability and activity. *Oncotarget* **5**, 1149–1156 (2014).
22. National Research Council, *Guide for the Care and Use of Laboratory Animals*, (National Academies Press, Washington, DC, ed. 8, 2011).
23. S. Itzkovitz, I. C. Blat, T. Jacks, H. Clevers, A. van Oudenaarden, Optimality in the development of intestinal crypts. *Cell* **148**, 608–619 (2012).
24. O. M. Enache *et al*., Cas9 activates the p53 pathway and selects for p53-inactivating mutations. *Nat. Genet.* **52**, 662–668 (2020).
25. F. Miller, Hemoglobin absorption by the cells of the proximal convoluted tubule in mouse kidney. *J. Biophys. Biochem. Cytol.* **8**, 689–718 (1960).
26. M. B. Burg, J. Orloff, Control of fluid absorption in the renal proximal tubule. *J. Clin. Invest.* **47**, 2016–2024 (1968).
27. M. I. Love, W. Huber, S. Anders, Moderated estimation of fold change and dispersion for RNA-seq data with DESeq2. *Genome Biol.* **15**, 550 (2014).
28. K. D. Sullivan *et al*., Mechanisms of transcriptional regulation by p53. *Cell Death and Differentiation* **25**, 133–143 (2018).
29. V. K. Mootha *et al*., PGC-1alpha-responsive genes involved in oxidative phosphorylation are coordinately downregulated in human diabetes. *Nat. Genet.* **34**, 267–273 (2003).
30. A. Subramanian *et al*., Gene set enrichment analysis: A knowledge-based approach for interpreting genome-wide expression profiles. *Proc. Natl. Acad. Sci. U.S.A.* **102**, 15545–15550 (2005).
31. H. Heberle, InteractiVenn: a web-based tool for the analysis of sets through Venn diagrams. *BMC Bioinformatics* **16**, 169 (2015).
32. C. Tanikawa *et al*., XEDAR as a putative colorectal tumor suppressor that mediates p53-regulated anoikis pathway. *Oncogene* **28**, 3081–3092 (2009).
33. M. Monte *et al*., The cell cycle-regulated protein human GTSE-1 controls DNA damage-induced apoptosis by affecting p53 function. *J. Biol. Chem.* **278**, 30356–30364 (2003).
34. M. Monte *et al*., Cloning, chromosome mapping and functional characterization of a human homologue of murine gtse-1 (B99) gene. *Gene* **254**, 229–236 (2000).
35. M. Fischer, Conservation and divergence of the p53 gene regulatory network between mice and humans. *Oncogene* **38**, 4095–4109 (2019).
36. K. Okamoto, D. Beach, Cyclin G is a transcriptional target of the p53 tumor suppressor protein. *EMBO J.* **13**, 4816–4822 (1994).
37. C. A. Brady *et al*., Distinct p53 transcriptional programs dictate acute DNA-damage responses and tumor suppression. *Cell* **145**, 571–583 (2011).
38. E. Ohashi *et al*., Error-prone bypass of certain DNA lesions by the human DNA polymerase kappa. *Genes Dev.* **14**, 1589–1594 (2000).
39. Y. Zhang, E. Park, C. S. Kim, J. H. Paik, ZNF365 promotes stalled replication forks recovery to maintain genome stability. *Cell Cycle* **12**, 2817–2828 (2013).
40. J. G. Jackson, O. M. Pereira-Smith, p53 is preferentially recruited to the promoters of growth arrest genes p21 and GADD45 during replicative senescence of normal human fibroblasts. *Cancer Res.* **66**, 8356–8360 (2006).
41. M. B. Kastan, O. Onyekwere, D. Sidransky, B. Vogelstein, R. W. Craig, Participation of p53 protein in the cellular response to DNA damage. *Cancer Res.* **51**, 6304–6311 (1991).
42. J. D. Siliciano *et al*., DNA damage induces phosphorylation of the amino terminus of p53. *Genes Dev.* **11**, 3471–3481 (1997).
43. S. Y. Shieh, M. Ikeda, Y. Taya, C. Prives, DNA damage-induced phosphorylation of p53 alleviates inhibition by MDM2. *Cell* **91**, 325–334 (1997).
44. O. Strobel *et al*., In vivo lineage tracing defines the role of acinar-to-ductal transdifferentiation in inflammatory ductal metaplasia. *Gastroenterology* **133**, 1999–2009 (2007).
45. N. Habbe *et al*., Spontaneous induction of murine pancreatic intraepithelial neoplasia (mPanIN) by acinar cell targeting of oncogenic Kras in adult mice. *Proc. Natl. Acad. Sci. U.S.A.* **105**, 18913–18918 (2008).
46. A. L. Haber *et al*., A single-cell survey of the small intestinal epithelium. *Nature* **551**, 333–339 (2017).
47. T. Stuart *et al*., Comprehensive integration of single-cell data. *Cell* **177**, 1888–1902.e21 (2019).
48. A. Butler, P. Hoffman, P. Smibert, E. Papalexi, R. Satija, Integrating single-cell transcriptomic data across different conditions, technologies, and species. *Nat. Biotechnol.* **36**, 411–420 (2018).
49. E. Papalexi, R. Satija, Single-cell RNA sequencing to explore immune cell heterogeneity. *Nat. Rev. Immunol.* **18**, 35–45 (2018).
50. C. Hafemeister, R. Satija, Normalization and variance stabilization of single-cell RNA-seq data using regularized negative binomial regression. *Genome Biol.* **20**, 296 (2019).
51. D. Menendez, A. Inga, M. A. Resnick, The expanding universe of p53 targets. *Nat. Rev. Cancer* **9**, 724–737 (2009).
52. W. S. el-Deiry *et al*., WAF1, a potential mediator of p53 tumor suppression. *Cell* **75**, 817–825 (1993).
53. J. W. Harper, G. R. Adami, N. Wei, K. Keyomarsi, S. J. Elledge, The p21 Cdk-interacting protein Cip1 is a potent inhibitor of G1 cyclin-dependent kinases. *Cell* **75**, 805–816 (1993).
54. T. A. Meyer *et al*., Sepsis and endotoxemia stimulate intestinal interleukin-6 production. *Surgery* **118**, 336–342 (1995).
55. S. J. van Deventer, J. W. ten Cate, G. N. Tytgat, Intestinal endotoxemia. Clinical significance. *Gastroenterology* **94**, 825–831 (1988).
56. R. Brosh *et al*., p53-dependent transcriptional regulation of EDA2R and its involvement in chemotherapy-induced hair loss. *FEBS Lett.* **584**, 2473–2477 (2010).
57. S. M. Post *et al*., A high-frequency regulatory polymorphism in the p53 pathway accelerates tumor development. *Cancer Cell* **18**, 220–230 (2010).
58. J. G. Jackson, O. M. Pereira-Smith, Primary and compensatory roles for RB family members at cell cycle gene promoters that are deacetylated and downregulated in doxorubicin-induced senescence of breast cancer cells. *Mol. Cell. Biol.* **26**, 2501–2510 (2006).
59. A. Dobin *et al*., STAR: Ultrafast universal RNA-seq aligner. *Bioinformatics* **29**, 15–21 (2013).
60. H. Li *et al*.; 1000 Genome Project Data Processing Subgroup, The sequence alignment/map format and SAMtools. *Bioinformatics* **25**, 2078–2079 (2009).
61. J. Harrow *et al*., GENCODE: The reference human genome annotation for the ENCODE project. *Genome Res.* **22**, 1760–1774 (2012).
62. S. Bai, E. Sei, N. E. Navin, Dissociation of Single Cell Suspensions from Human Breast Tissues (2018). https://www.protocols.io/view/dissociation-of-single-cell-suspensions-from-human-t3geqjw. Accessed 21 October 2019.